Hindawi
Shock and Vibration
Volume 2023, Article ID 4640726, 20 pages
https://doi.org/10.1155/2023/4640726

Research Article

Field Measurement and Energy Analysis of Ground-Borne Vibration around High-Speed Railway Viaduct

Yanmei Cao, Qi Xiang, Boyang Li, and Zhaoyang Li

School of Civil Engineering, Beijing Jiaotong University, Beijing 100044, China

Correspondence should be addressed to Qi Xiang; 21121126@bjtu.edu.cn

Received 19 May 2023; Revised 27 August 2023; Accepted 11 September 2023; Published 20 September 2023

Academic Editor: Madalina Dumitriu

In order to investigate the vibration characteristics and propagation mechanism of ground vibrations induced by high-speed train passing through the viaduct, a field experiment is carried out, and the measured data is deeply analyzed. Besides the independent time domain and frequency domain analysis, the continuous wavelet transform (CWT) is performed on the vibration signal to analyze the energy distribution characteristics of ground vibrations from the view of time-frequency synchronous analysis. The experimental results show that the ground vibrations have obvious nonstationary characteristics; the first dominant frequency of ground vibration is concentrated between 40–55 Hz, which is affected by the excitation frequency of the train wheel axle and the peak frequency of wheel-rail interaction force. The ground vibrations attenuate gradually as the distance from the railway track increases, in which the high-frequency components above 50 Hz attenuate faster, low-frequency components below 8 Hz continuously decay in the near field, and medium-frequency components within 8–50 Hz decay slower with a longer transmission distance. Compared with traditional methods, time-frequency synchronous analysis of ground vibration signals is more accurate and intuitive, and the CWT can be used as a promising method in the analysis of ground-borne vibration from high-speed railway.

1. Introduction

With the massive construction and rapid development of high-speed railways (HSR) around the world, the environmental vibration problems around the HSR lines are becoming increasingly serious [1]. The environmental vibration and noise caused by trains passing through residential areas may affect people's daily lives and health [2, 3]. Therefore, the measurement, evaluation, and reduction of the hazards of environmental vibration have been paid increasing attention [4]. In the existing high-speed railway lines, a large part of the lines is composed of bridges [5], so it is of great significance to study the mechanism and propagation law of environmental vibration around high-speed railway bridges [6]. For the environmental vibration caused by elevated railway, researchers have conducted extensive and detailed research [7]. The research methods mainly include theoretical analysis, numerical simulation, and field test, in which the field test has incomparable advantages due to its consistency with the actual vibration situation.

By means of field tests, Xia et al. [8] studied the ground vibration of the surrounding site caused by the elevated section of Beijing Metro Line 5 and summarized the propagation laws of ground vibration along different directions. Zhai et al. [9] measured the ground vibration response caused by high-speed trains traveling at 300–400 km/h through the roadbed section and found the influence of vehicle parameters on the vibration response amplitude. In order to survey the influence of the soil condition on ground vibrations, Niu et al. [10] selected a typical loess area and conducted field tests on the ground vibration caused by the operation of the Datong-Xi'an high-speed railway. Wang et al. [11, 12] found that the main frequency of vertical soil acceleration induced by HSR is an integer multiple of the train loading frequency generated by the center distance of two adjacent carriages. Li and Liu [13] conducted a field measurement in the Guanhu metro depot of Guangzhou city and proposed a method based on the operational transfer path analysis (OTPA) and singular value decomposition (SVD) to obtain the vibration transmission characteristics

and quantify vibration contribution values along different transmission paths. In order to improve the accuracy of vibration prediction, Liu et al. [14] presented a methodology implemented in the frequency domain to predict ground-borne vibration caused by the passage of trains in a curved tunnel, and field tests were conducted in the curved tunnel of Beijing Metro Line 15 to demonstrate the effectiveness of the prediction method. Some researchers also tried to combine experimental data and numerical models [15–17] to obtain a hybrid analysis method. Moreover, some neural network models are trained by actual test data to obtain a more accurate vibration prediction method [18–20].

In dealing with the vibration data from field measurement, the analysis based on time history and Fourier spectrum is the most commonly used. Although the Fourier transform is an effective method in reflecting frequency characteristics of ground vibration signal, it cannot accurately express the nonstationary characteristics of railway traffic-induced ground vibration nor can it reflect the change of the signal spectrum with time. Therefore, the traditional Fourier transform is somehow limited. In case of practical need, the continuous wavelet transform (CWT) [21, 22] was derived from the short-time Fourier transform (STFT). Caprioli et al. [23] presented the limitations of the STFT and further illustrated that the CWT of a signal is a more promising technique. Garinei et al. [24] also obtained the effectiveness and prospects of CWT in analyzing transient signals. As a convenient and efficient signal processing technique, the CWT can capture the signal's frequency while preserving its time information and has been applied in various fields [25–27]. For example, some researchers used time-frequency analysis of CWT to detect and diagnose train and track faults with high accuracy [23, 28–31] to ensure the operation safety of train; the time-frequency analysis combined with convolutional neural network technique was applied to the detection of machine faults [32, 33]. By using the modified Littlewood-Paley (MLP) wavelet basis, Cantero et al. [34] analyzed the time-frequency response of the bridge vibration caused by the running train and found that the frequency spectrum of the bridge vibration affected the vehicle's speed and axle configuration as well as nonlinear behavior of the axle.

In addition to the time-frequency analysis by the CWT technique, some scholars [35–37] have also conducted energy analysis based on time-frequency information of signals to further compensate for the shortcomings of traditional analysis methods. Zhou and Adeli [38] proposed wavelet energy spectra for time-frequency localization of seismic signals, and the results showed that the wavelet energy spectrum can be regarded as a microscope for looking into the time-frequency characteristics of vibration signals, which is helpful for signal analysis.

In this paper, an on-site experiment of the ground-borne vibration around the HSR viaduct is carried out, and the measured ground vibration signals are analyzed from different angles, including time domain analysis, frequency domain analysis, time-frequency domain analysis, and energy analysis. By combining traditional analysis methods with new CWT analysis methods, more comprehensive characteristics and propagation laws of ground vibration caused by the elevated high-speed railway are obtained. At the same time, the advantages and development prospects of CWT over traditional analysis methods are also illustrated.

2. Wavelet Transform

As an excellent tool for time-frequency analysis, the wavelet transform [39] proposes the core idea of the scaling and translation of signals, and it can be used to analyze signals with different frequencies by using adaptable window lengths [40]. Compared to the STFT, the wavelet transform has better time-frequency window characteristics, making it highly adaptable to nonstationary signals, and provides a good balance between frequency and time resolution in signal processing. Herein, the continuous wavelet transform (CWT), one of the most popular tools in wavelet transform, is adopted. The CWT of a function $v(t)$ can be defined as follows [39]:

$$W_v(a,b) = \langle f, \varphi_{a,b} \rangle = \frac{1}{\sqrt{|a|}} \int_{-\infty}^{+\infty} v(t) \varphi_{a,b}^* \left(\frac{t-b}{a} \right) \mathrm{d}t, \quad (1)$$

where W_v is the wavelet transform result of the function $v(t)$; a denotes the scaling factor controlling the wavelet expansion; b is the shifting factor representing the position of the wavelet; $\varphi_{a,b}(t)$ is the wavelet basis function; $\varphi_{a,b}^*(t)$ denotes the conjugate operation performed on $\varphi_{a,b}(t)$.

The different wavelet basis functions $\varphi_{a,b}(t)$ can be obtained by scaling and translating the same basis wavelet $\varphi(t)$, which can be written as follows:

$$\varphi_{a,b}(t) = \frac{1}{\sqrt{a}} \varphi \left(\frac{t-b}{a} \right). \quad (2)$$

In general, the wavelet coefficients are expressed in terms of a scale factor a. The relationship between the scale a and the actual frequency f_a is as follows [41]:

$$f_a = \frac{f_s f_c}{a}, \quad (3)$$

where f_s is the sampling rate of the vibration signal; f_c is the central frequency of the wavelet master function.

Based on the basic principle of CWT, the time-frequency energy $E_{a,b}$ of the signal wavelet can be expressed as follows [38]:

$$E_{a,b} = \frac{|W_v(a,b)|^2}{\pi}. \quad (4)$$

Since the frequency range of ground vibrations caused by passing HSR trains is mainly within 200 Hz [42], the maximum frequency of the CWT is set to 200 Hz in the paper.

Figure 1 gives an example of using CWT to process the measured ground vibration signal, in which Figure 1(a) is a 3D surface diagram in the time-frequency domain, and Figure 2(b) is the 2D time-frequency diagram obtained by CWT.

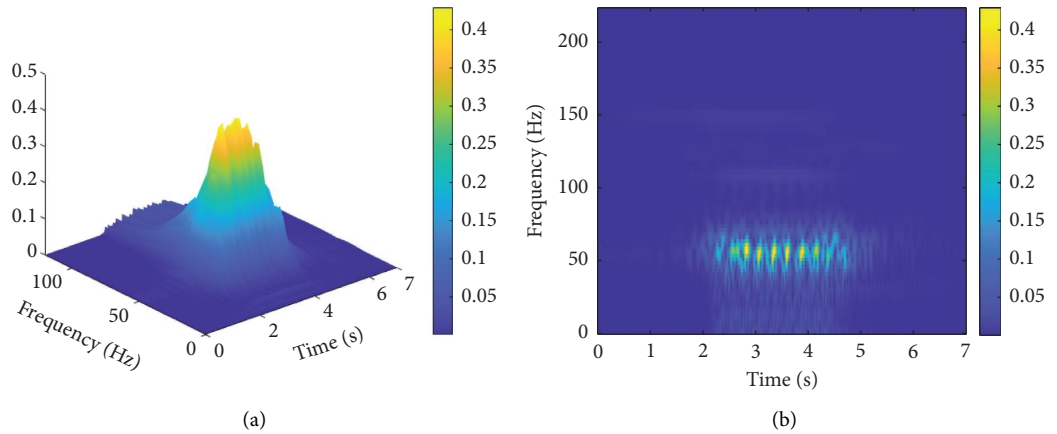

(a) (b)

Figure 1: Example of time-frequency analysis by CWT. (a) 3D time-frequency diagram. (b) 2D time-frequency diagram.

Figure 2: Experimental site.

3. Field Experiment of Ground-Borne Vibration

3.1. Site Overview. An elevated section located at Yuanping West to Yangqu West of the Datong to Xi'an high-speed railway (Daxi HSR) is selected as the experimental site, and the train speed ranges from 250 km/h to 385 km/h. The bridge in the test section has a standard 32 m double track concrete box girder (Figures 2 and 3), and the height and width of the beam section are, respectively, 3.08 m and 12 m. More details of the cross section of the beam and pile group foundation are shown in Figure 3. The first vertical bending eigenfrequencies of the box girder is 9.23 Hz, the first torsional eigenfrequencies is 15.36 Hz, and the first lateral frequency is 24.1 Hz [43].

Around the HSR bridge, an open farmland with flat terrain was selected as the experimental free field, as shown in Figure 2.

3.2. Layout of Measuring Points. The layout of the measuring points for the free field vibration test is shown in Figure 4. The track on the side relatively far from the free field is called the far track and that closer to the field is called the near track. The intersection between the center line of the bridge pier and the horizontal line of the ground is set as the coordinate origin O, with the train running direction for the x-axis, perpendicular to the train running direction for the y-axis, and vertical down for the z-axis. The x, y, and z directions are also known as the longitudinal, transverse, and vertical directions. As shown in Figure 4, the acceleration sensors of $1^{\#}$ and $2^{\#}$ are laid on the beam bottom and the pier top, respectively. Besides, the measurement points ($3^{\#}$–$9^{\#}$) of ground vibration are arranged with different spacing in the side of the bridge pier along the y-axis direction.

In the experiment, all acceleration sensors are of the 941B type (Institute of Engineering Mechanics, China Earthquake Administration. Range 0–20 g, frequency response range 0.25–80 Hz) with a sampling frequency of 512 Hz. Three acceleration sensors are simultaneously installed at each measuring point to measure the vibration acceleration in the x, y, and z directions in Figure 4. In addition, the 28-bit network distributed synchronous acquisition instrument INV3020S designed by Beijing

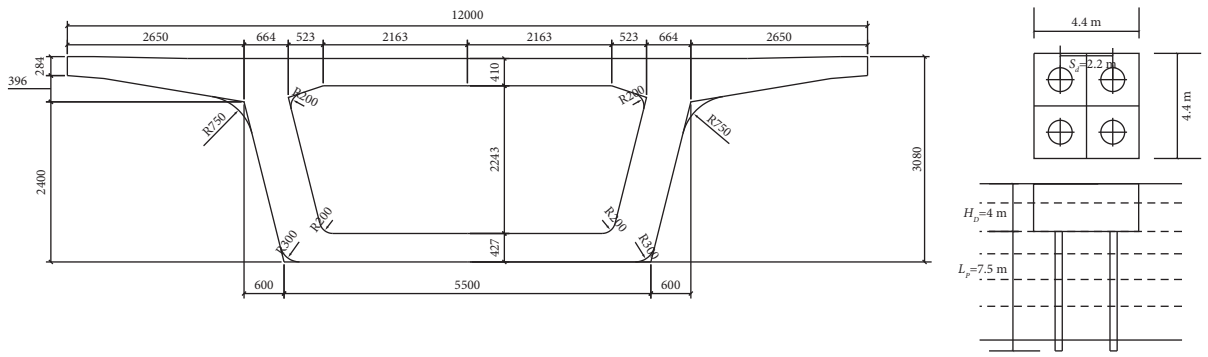

Figure 3: Schematic diagram of the bridge and pile foundation. (a) Cross section of box girder (unit: mm). (b) Pile group foundation.

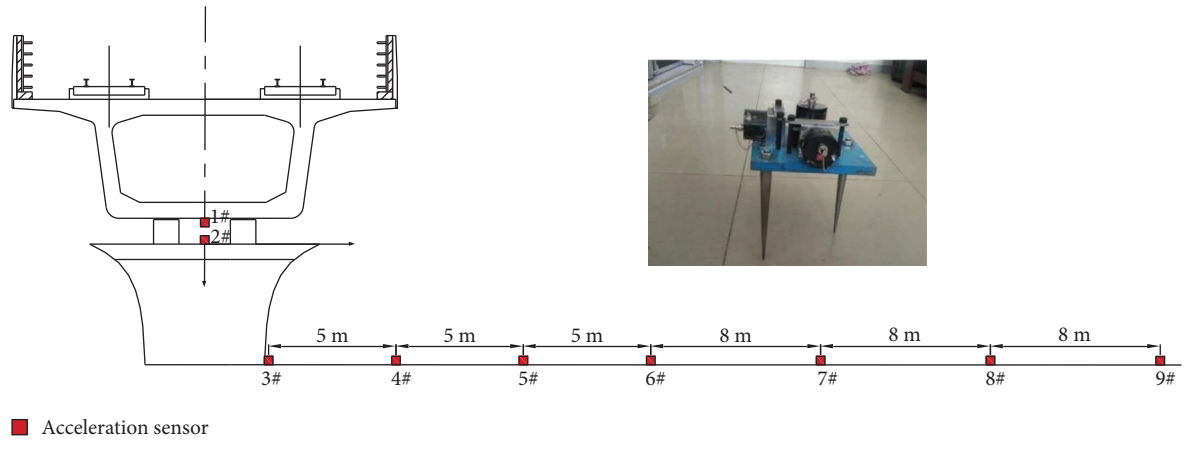

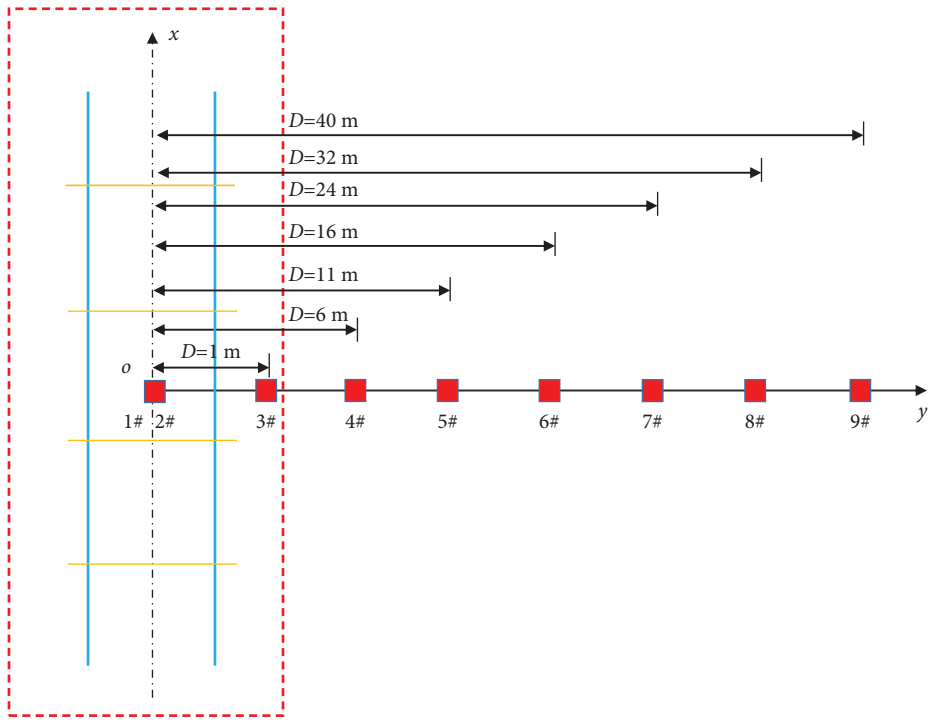

Figure 4: Arrangement of measuring points in the experiment. (a) Elevation view. (b) Plan view.

Dongfang Vibration and Noise Research Institute is used for data acquisition in cooperation with the DASP-V10 operation software.

3.3. Test Conditions. The running high-speed train during the test is the CRH380A, with an axle weight of approximately 14 t and an 8-car formation, as shown in Figure 5(a). The wheelset mass of CRH380A is about 2000 kg. In addition, the characteristic length of the test train is given in Figure 5(b), with bogie wheelbase $L_1 = 2.5$ m, the central distance between adjacent bogies $L_2 = 7.625$ m of adjacent vehicles, the central distance between front and rear bogies $L_3 = 17.375$ m for the same vehicle, and overall length $L_4 = 25$ m for a single vehicle. The CRST-II slab ballastless track is laid on the bridge (Figure 5(c)), in which the rail mass per length is 60 kg/m and the rail pad stiffness is 900 MN/m.

4. Characteristics and Transmission Law of Ground Vibrations

4.1. Removal of Background Vibration. While the accelerometer picks up the vibration signal caused by the passage of the train, it also picks up background vibrations caused by ambient vibrations such as ground pulsations. In the subsequent processing of the test data, the influence of background vibration on HSR-induced ground vibrations needs to be removed first. During the field test, a number of background vibration data were collected. Take the vertical ground vibration at $D = 24$ m as an example, the collected original ground vibration with an HSR train passing through the bridge at the speed of 337 km/h and the collected background vibration without train passing are shown in Figures 6(a) and 6(b), respectively.

To remove the disturbance of background vibration, both the measured ground vibration and the measured background vibration are transformed by the fast Fourier transformation to obtain the Fourier spectrum (Figures 6(a) and 6(b)). It can be clearly seen that there is a disturbance at the frequency of 49.8 Hz from the ambient vibration. Then, the amplitudes of two spectra corresponding to the same frequency are subtracted to remove the background vibration components. After the treatment of the background vibration, the real vertical ground acceleration of $D = 24$ m can be obtained, as shown in Figure 6(c).

4.2. Vibration Characteristics Analysis. The measured ground vibration induced by an HSR train running at the speed of 337 km/h is taken as an example.

4.2.1. Histories and Frequency Spectra of Beam Bottom and Pier Top. Figure 7 shows the time histories and Fourier spectra of the vertical vibration acceleration at the beam bottom and on the top of the pier.

As shown in Figure 7(a), the periodic loading phenomenon with nine obvious peaks can be observed from the history curves, which is due to the train composition with a total of eight segments, and the peaks correspond to axle loads. In addition, Figure 7(b) reflects that the vibration energy of the beam bottom is mainly distributed between 30 Hz and 100 Hz, but that greater than 50 Hz slightly dissipates from the beam bottom to the pier top because of the energy consumption of the beam structure and support system.

4.2.2. Histories and Frequency Spectra of Ground Vibrations. The vertical acceleration histories and frequency spectra of $D = 1$ m, 6 m, 11 m, 16 m, 24 m, and 32 m on the ground surface are shown in Figures 8(a) and 8(b). Simultaneously, the vertical ground velocities at $D = 1$ m, 6 m, and 11 m are also shown in Figure 8(c).

Generally, either acceleration or velocity can be adopted as the evaluation index of ground vibration. According to international standards ISO 14837-1 [44] and ISO8041-1 [45], the metrics for evaluating ground vibration and human whole-body vibration are usually acceleration, so the subsequent response representations are mainly based on acceleration signals. As you can see from Figures 7 and 8, the vertical acceleration amplitude of HSR train-induced vibration shows a very obvious attenuation from the beam bottom to $D = 11$ m on the ground, and the attenuation tends to gradually slow down with the distance increase from $D = 11$ m to $D = 40$ m.

On the other hand, the vertical acceleration spectrum of the beam bottom ($D = 0$ m) has a wide frequency distribution (0–100 Hz). When the vibration is transferred from the bridge deck to the pier and then from the pier to the ground, the high-frequency components above 80 Hz in the vibration are greatly attenuated. From the vertical acceleration spectrum of each measurement point on the ground, it can be seen that as the vibration wave propagates in the soil, the frequency components of 50–100 Hz are greatly filtered by soil media and rapidly attenuate, while those vibration components between 8 Hz and 50 Hz decay gradually and can be transmitted to a farther distance. Although the vibration components below 8 Hz also keep continuous decay, the attenuation rate is less than the 50–100 Hz components and almost invariant behind $D = 11$ m. So, the ground vibrations with different frequencies have different decay characteristics. Hereafter, three frequency ranges of around 0–8 Hz, around 8–50 Hz, and around 50–100 Hz are distinguished by low frequencies, medium frequencies, and high frequencies [46].

The different decay characteristics are closely related to soil properties. Above all, the soil damping has a significant energy consumption effect on the propagation of high-frequency vibration components. Next, the vibration of the layered soil has often a low-frequency cutoff with small amplitudes at the low frequencies. Then, the attenuation of mid-frequency vibration is between these two situations, so it has little attenuation during the transmission process and plays a dominant role in the far field [47]. Moreover, it should be noted that, in the normal operation of high-speed railway, the irregularities of the vehicle (such as out-of-round wheels) are an important part of the high-frequency excitation, while the track irregularities and train-track dynamic interaction can explain the medium-frequency ground vibrations to a certain extent [48].

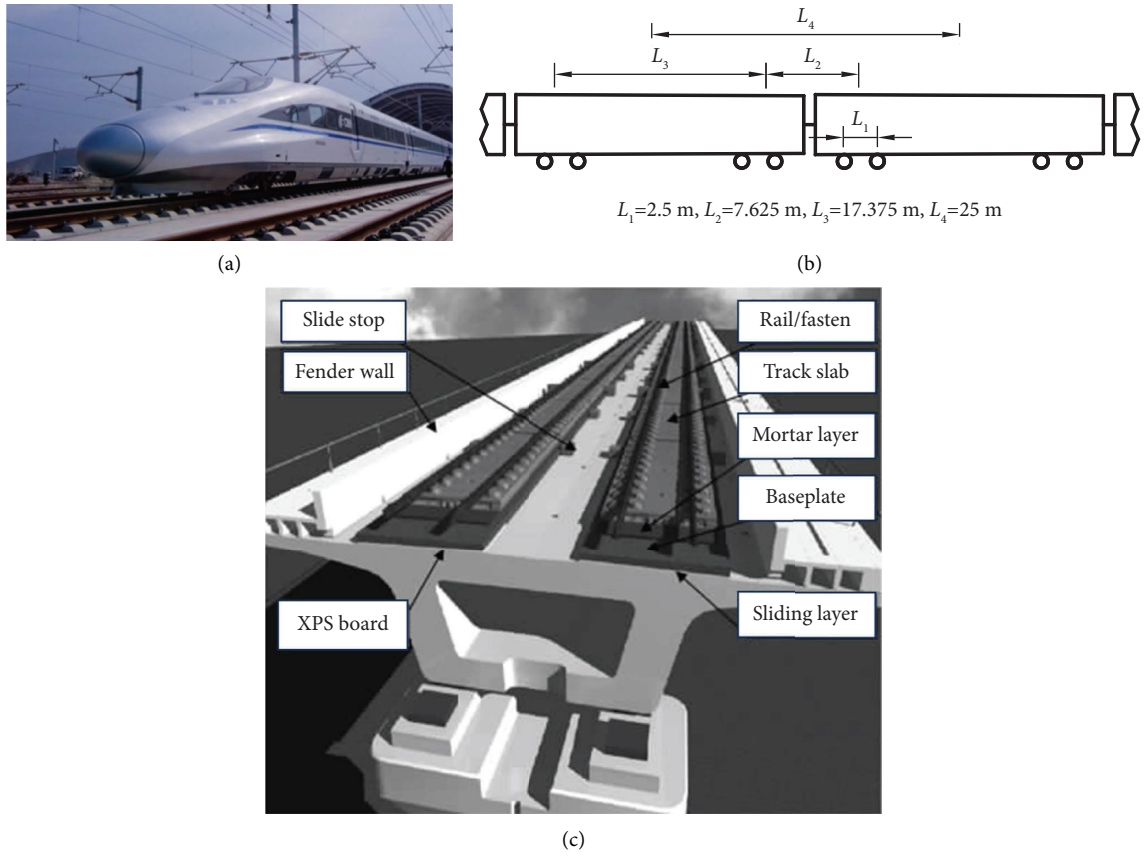

Figure 5: Type and parameters of the HSR train. (a) CRH380A high-speed train. (b) Characteristic lengths of the HSR train. (c) CRTSII-track slab.

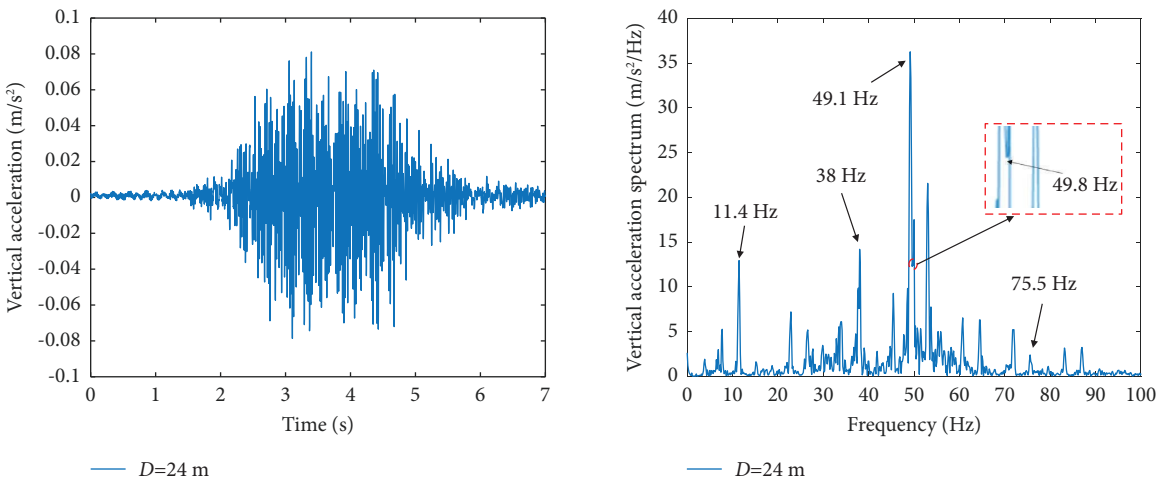

Figure 6: Continued.

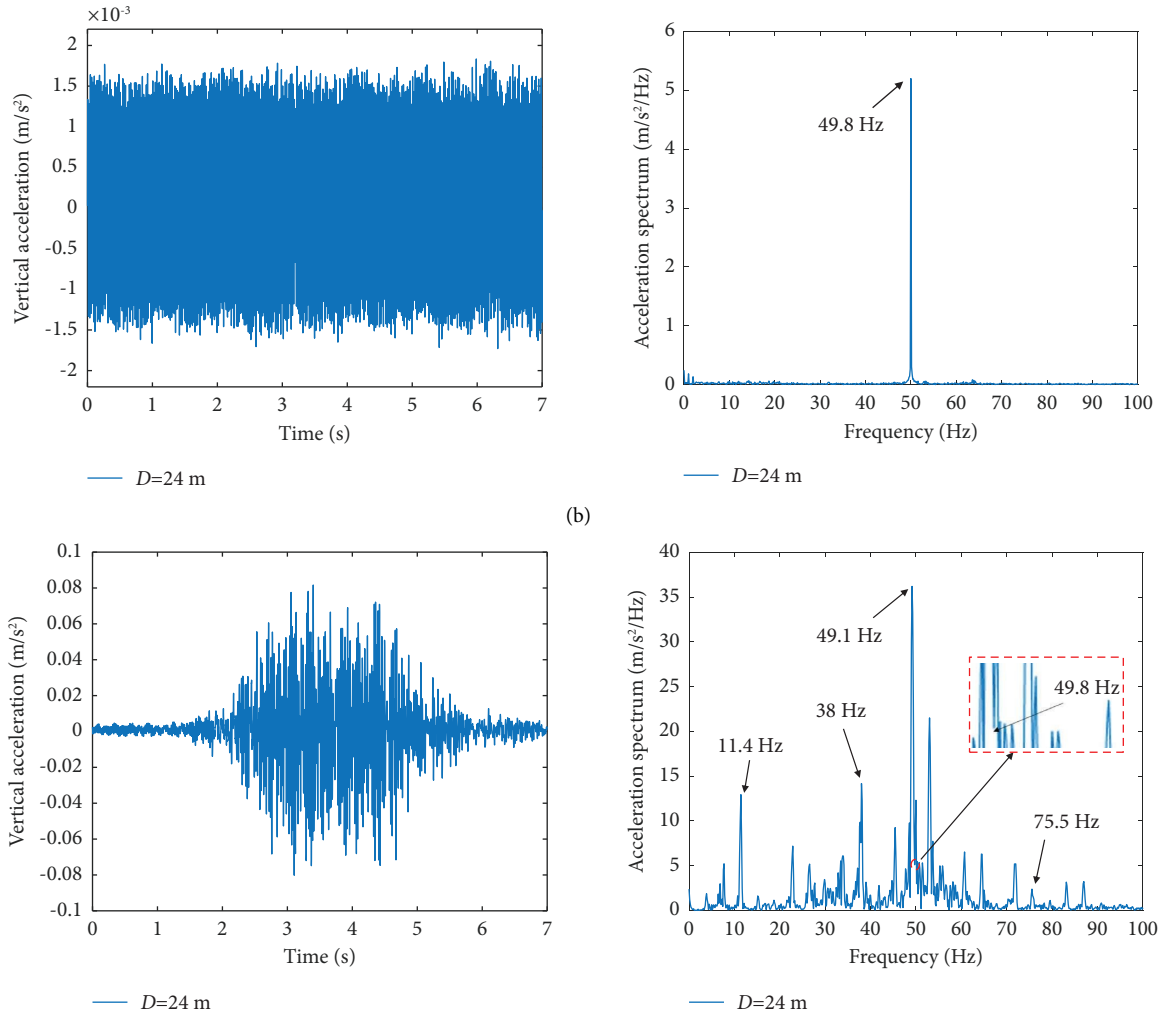

FIGURE 6: Background vibration treatment of ground acceleration ($D = 24$ m). (a) Collected original ground vibration. (b) Background vibration. (c) Ground vibration after removing background vibration.

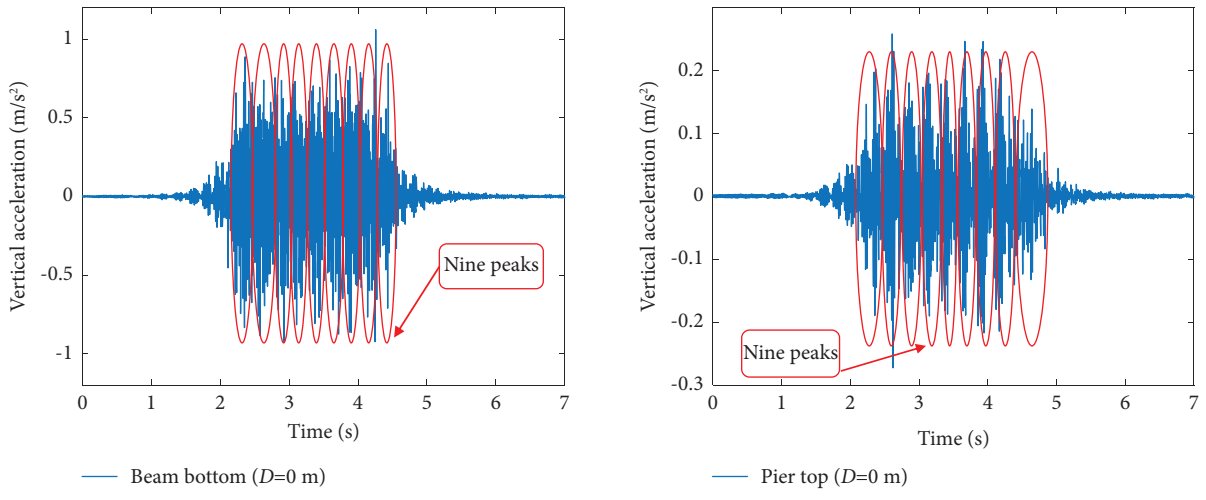

FIGURE 7: Continued.

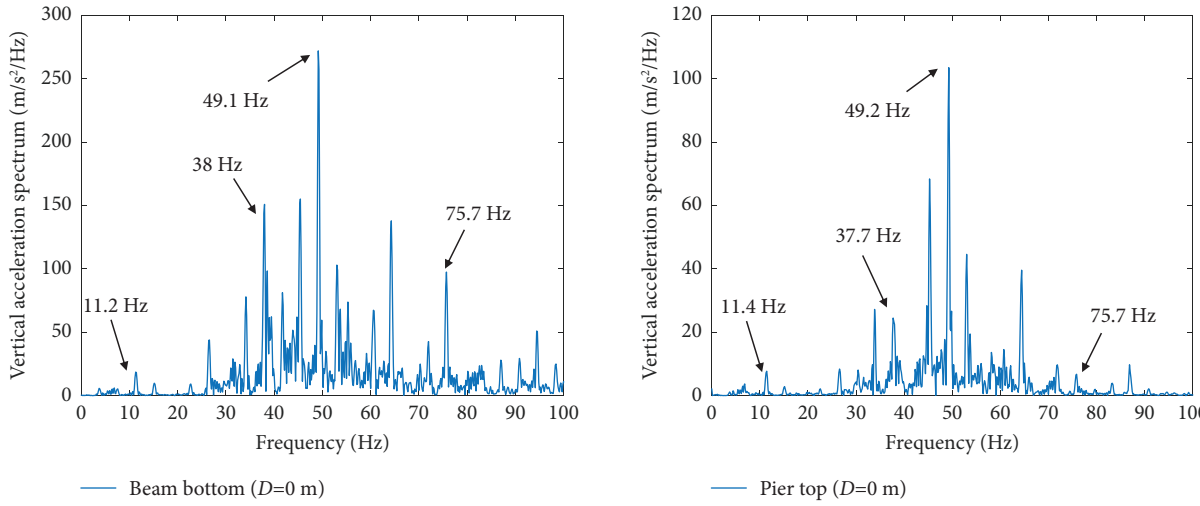

(b)

Figure 7: Histories and spectra distribution of vertical vibrations at beam bottom and on pier top. (a) Time histories. (b) Frequency spectra.

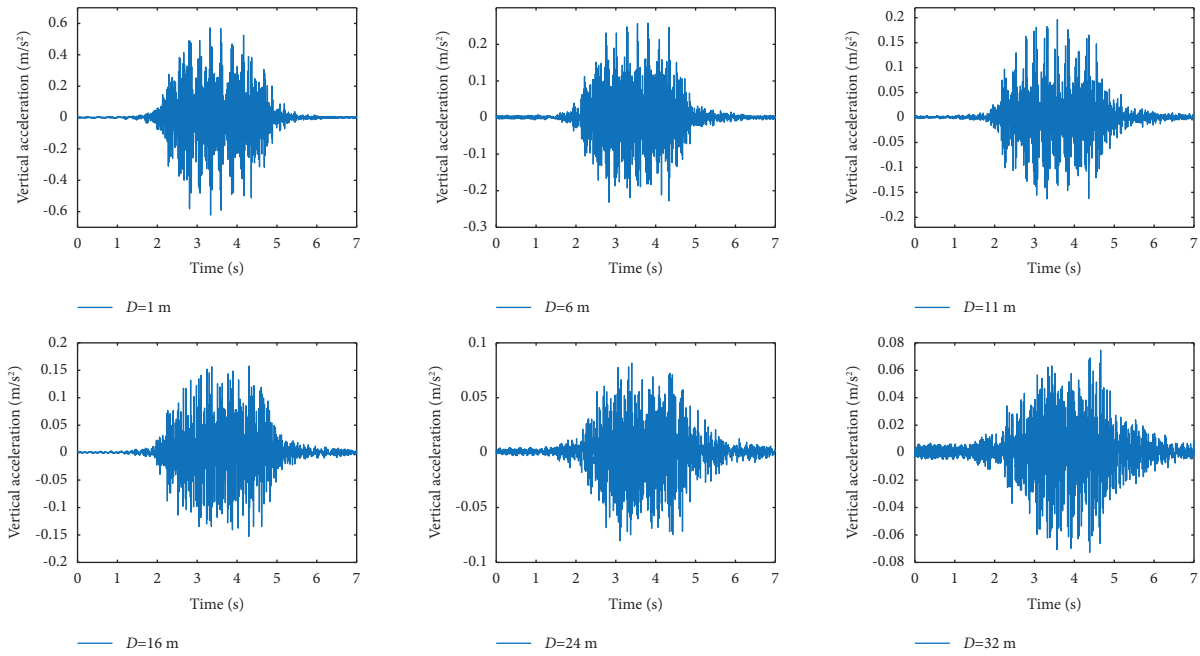

(a)

Figure 8: Continued.

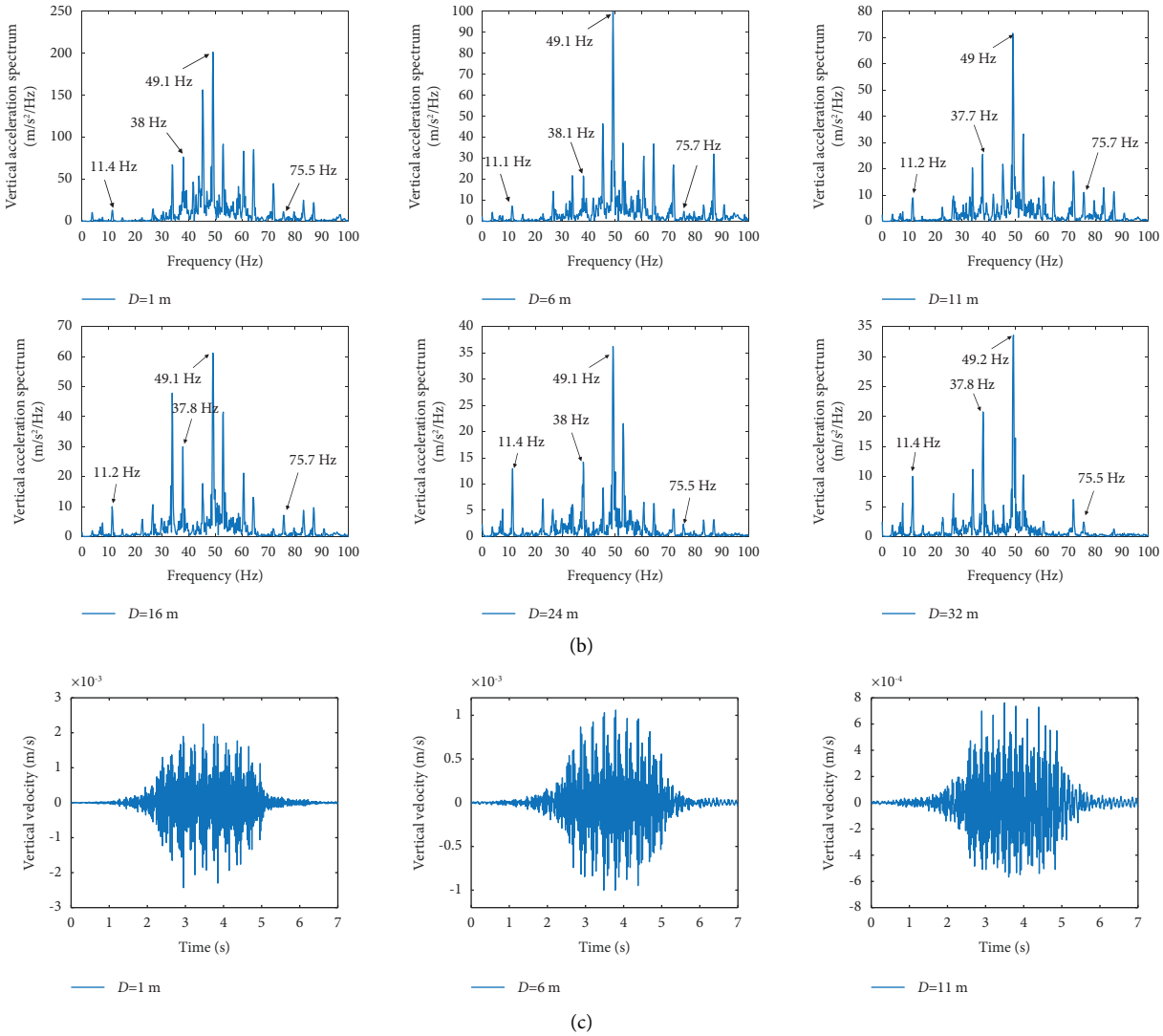

FIGURE 8: Histories and spectra of vertical ground acceleration and velocity ($v = 337$ km/h). (a) Vertical acceleration histories of ground vibrations. (b) Vertical acceleration spectra of ground vibrations. (c) Vertical velocity histories of ground vibrations.

From the acceleration spectrum of vertical ground vibration, it can be seen that there are some dominant frequencies. First, the first dominant frequency is about 49.1 Hz. According to the existing research [49], the vibration caused by wheel-rail forces under the effect of track irregularity will have a corresponding spectral component, and the peak frequency f_m of wheel-rail force can be approximated to be:

$$f_m = \frac{1}{2\pi}\sqrt{\frac{2\sqrt{2}\,(EI)^{0.25}S^{0.75}k_{\mathrm{H}}}{\left[2\sqrt{2}\,(EI)^{0.25}S^{0.75}+k_{\mathrm{H}}\right]m_w}}, \tag{5}$$

where EI is the bending stiffness of the rail; S is the supporting stiffness of the rail per linear metre; k_H is the simplified spring stiffness of wheel-rail linear Hertzian contact; m_w is the mass of a single wheel. The peak frequency of the wheel-rail force in this test is calculated to be 48.32 Hz by equation (5), which is very close to the peak frequency in the spectrogram.

Second, other dominant frequencies are related to the periodic excitation frequency from the train. According to the existing research by Zhai et al. [9] and Ju et al. [50], the periodic excitation frequency from the running train can be calculated by $f_i = nv/(3.6 * L_i), i = 1, 2, 3, 4, n = 1, 2, 3\ldots$, where v is the train speed (unit: km/h) and L_i is the characteristic length of the train (unit: m). According to the characteristic dimensions of the train (Figure 5), when n equals one, the periodic excitation frequencies are, respectively, $f_1 = 37.4$ Hz, $f_2 = 12.3$ Hz, $f_3 = 5.4$ Hz, and $f_4 = 3.74$ Hz, in which f_1 is very close to the peak value of 38 Hz marked in the spectrogram. Similarly, f_2, $7f_3$, $4f_2$, and $2f_1$ are also very close to the peaks of 11.4 Hz, 38 Hz, 49 Hz, and 75.5 Hz in the spectrogram (Figure 8(b)). This indicates

that the train loading frequency f_i and its integer multiplier have a significant impact on the dominant frequencies of ground vibration.

4.2.3. Time-Frequency Characteristics by CWT. In order to observe the change of the spectrum with the passing time of the train, the Morse wavelet is utilized in the CWT of the signals. At the same time, it is also possible to perform a multiangle analysis of vibration characteristics. Figure 9 shows the time-frequency diagram of each measuring point.

From the time-frequency diagram of vertical acceleration at the beam bottom, it can be seen that the vibration energy of the beam bottom mainly distributes in the range of 30–100 Hz, and the peak frequency occurs near 50 Hz, which is consistent with the result of Fourier spectrum (Figure 8). Moreover, the vibration energy at the pier top is concentrated around 50 Hz, and the percentage of frequency components below 30 Hz at the pier top is smaller than the beam bottom, which can be indicated from the color brightness of the time-frequency energy map as shown in Figure 9.

For the time-frequency diagrams of ground vibrations, the time and frequency at which the train passes correspond to the area with the highest energy, so the number of brightest areas in Figure 9 corresponds to the train formation, reflecting nine energy accumulation points in the time-frequency diagrams. In addition, it can be observed from Figure 9 that the time-frequency signal of the ground vibration response shows obvious shock characteristics and the vibration energy mainly concentrates in some local frequency bands. The peak frequency is concentrated in the vicinity of 50 Hz, corresponding to the excitation frequency of wheel-rail force as shown in equation (5). Moreover, as the distance between measuring points increases, the energy decreases and the impact characteristics of ground vibration weaken gradually. By comparing Figures 8 and 9, one can find that the ground vibration characteristics obtained by the CWT analysis method have a good agreement with those by Fourier spectrum analysis, but the results of CWT are more intuitive, which can reflect the change of spectrum characteristics with time.

4.2.4. Ground Vibrations at Different Train Speeds. In the experiment, the vibration signals were collected under six different train speeds of 200 km/h, 250 km/h, 290 km/h, 300 km/h, 320 km/h, and 337 km/h. Figure 10 gives the ground vibrations of $D = 11$ m and $D = 16$ m under $v = 200$km/h, $v = 300$km/h, and $v = 337$km/h. It can be seen that the higher train speed generally induces the greater ground vibration amplitudes. Figure 11 shows the time-frequency diagrams of ground vibration at $v = 200$ km/h and $v = 300$ km/h, and the energy concentration frequency band can be observed obviously.

According to $f_i = nv/(3.6 * L_i), i = 1, 2, 3, 4, n = 1, 2, 3 \ldots$, the wheel-axle excitation frequencies f_1 are 37.4 Hz ($v = 337$km/h), 22.2 Hz ($v = 290$km/h), and 33.3 Hz ($v = 300$km/h). By comparing the peak frequencies in Figures 9 and 11, it is easy to find that the spectral characteristics of the ground vibration are greatly influenced by the wheel-axle excitation frequency f_1 and the peak frequency $f_m = 48.32$ Hz of wheel-rail force together.

In order to further explore the impact of train speed on the vibration response in the frequency domain, the vertical vibration acceleration level (VAL_Z) with one-third octave band [45] at different train speeds is conducted, as shown in Figure 12.

From Figure 12, it can be seen that the maximum vibration levels at different train speeds concentrate on about 49 Hz for all the measurement points. This is very consistent with the conclusions in 4.2.2 and 4.2.3. Overall, the vibration level increases with frequency before 50 Hz and decays rapidly after 50 Hz, in which the vibration fluctuates between increasing and decreasing between 4 Hz and 16 Hz. Under different train speeds, the tendency of vibration response with frequency can maintain good consistency before 4 Hz and after 16 Hz, but it changes with the change of train speed between 4 Hz and 16 Hz (the amplification can be seen in Figure 13).

It can be seen from Figure 13 that the variation tendency of ground vibrations with 4–16 Hz is the same at $v = 200$km/h and $v = 250$km/h, and it is also approximately the same at $v = 290$km/h, $v = 300$ km/h, and $v = 320$km/h, but there is obvious difference at $v = 337$km/h. Similarly, it can be seen that there may be a "watershed" between 250 km/h and 290 km/h, as well as between 320 km/h and 337 km/h, resulting in the variation relationship between vibration response and frequency with the increase of train speed. This "watershed" may be related to certain parameters of the soil layer.

4.3. Wavelet Energy Analysis of Ground Vibrations. By superimposing the CWT amplitude of the vibration signal, the wavelet energy curves of ground vibrations at each moment can be obtained, as illustrated in Figure 14.

Figure 14 gives the specific energy distribution at each single moment. At $D = 1$ m, the carriage number of trains corresponding to the peak section can be obviously seen, and the time of each train passing through the measurement point can also be observed. For the vibrations at different distances on the ground, the peaks of the vibration curve are consistent in time when the train is passing.

In order to fully demonstrate the vibration energy characteristics, the results of the wavelet transform are further processed (accumulating over time), and the cumulative curves of the main energy bands can be obtained in the time domain, as shown in Figure 15.

As shown from the dashed lines in Figure 15, there are nine obvious "step" jumps (between each pair of dashed lines) in the energy accumulation curves of the $D = 0$ m to $D = 40$ m. The "step" jump indicates the local concentration of vibration energy, which corresponds to eight carriages in this test and the nine energy accumulation points (Figure 7) of the time-frequency energy spectrum. It shows that the local energy concentration is caused by different train compartments passing through the coordinate origin O,

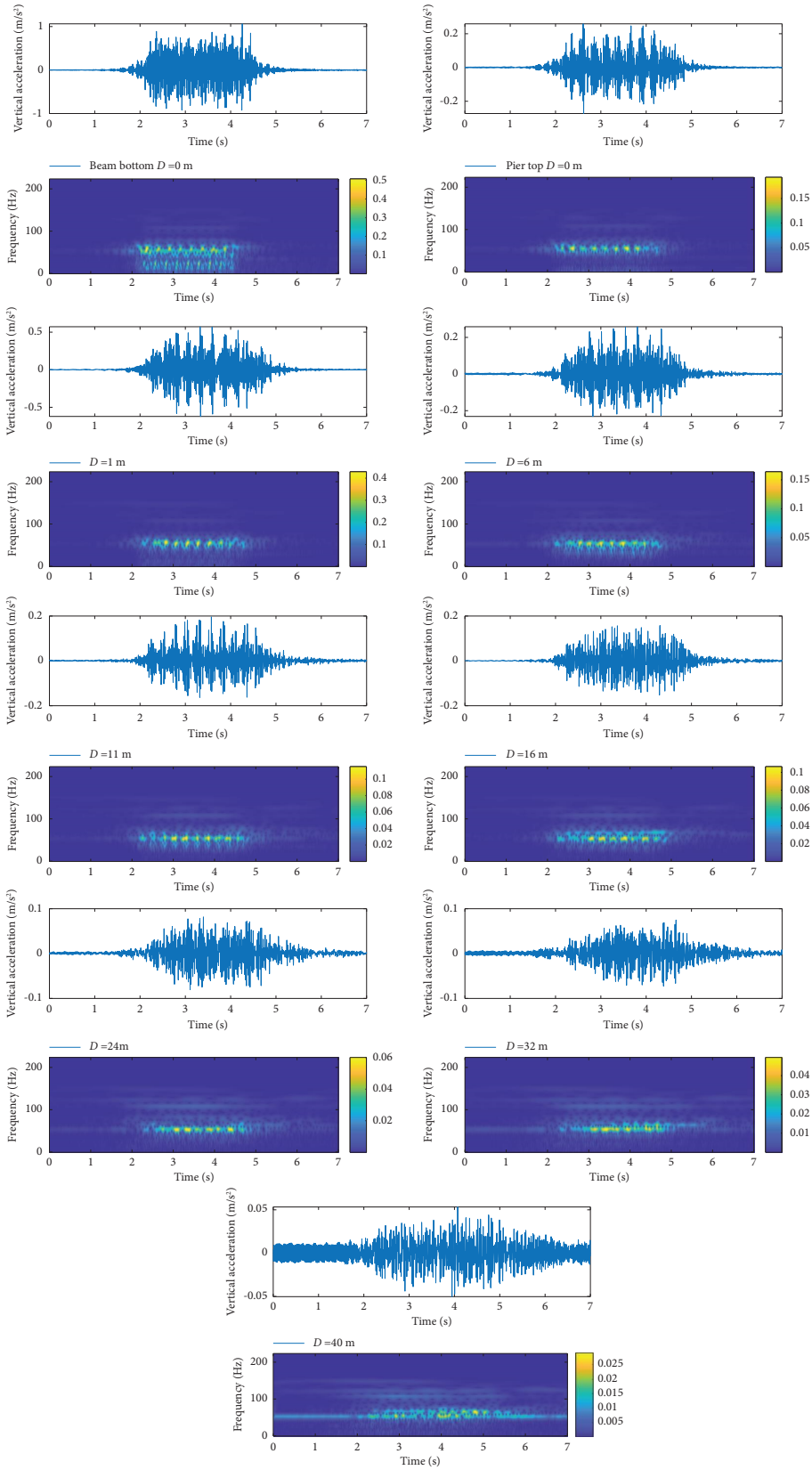

Figure 9: Time-frequency distribution of vertical acceleration ($v = 337$ km/h).

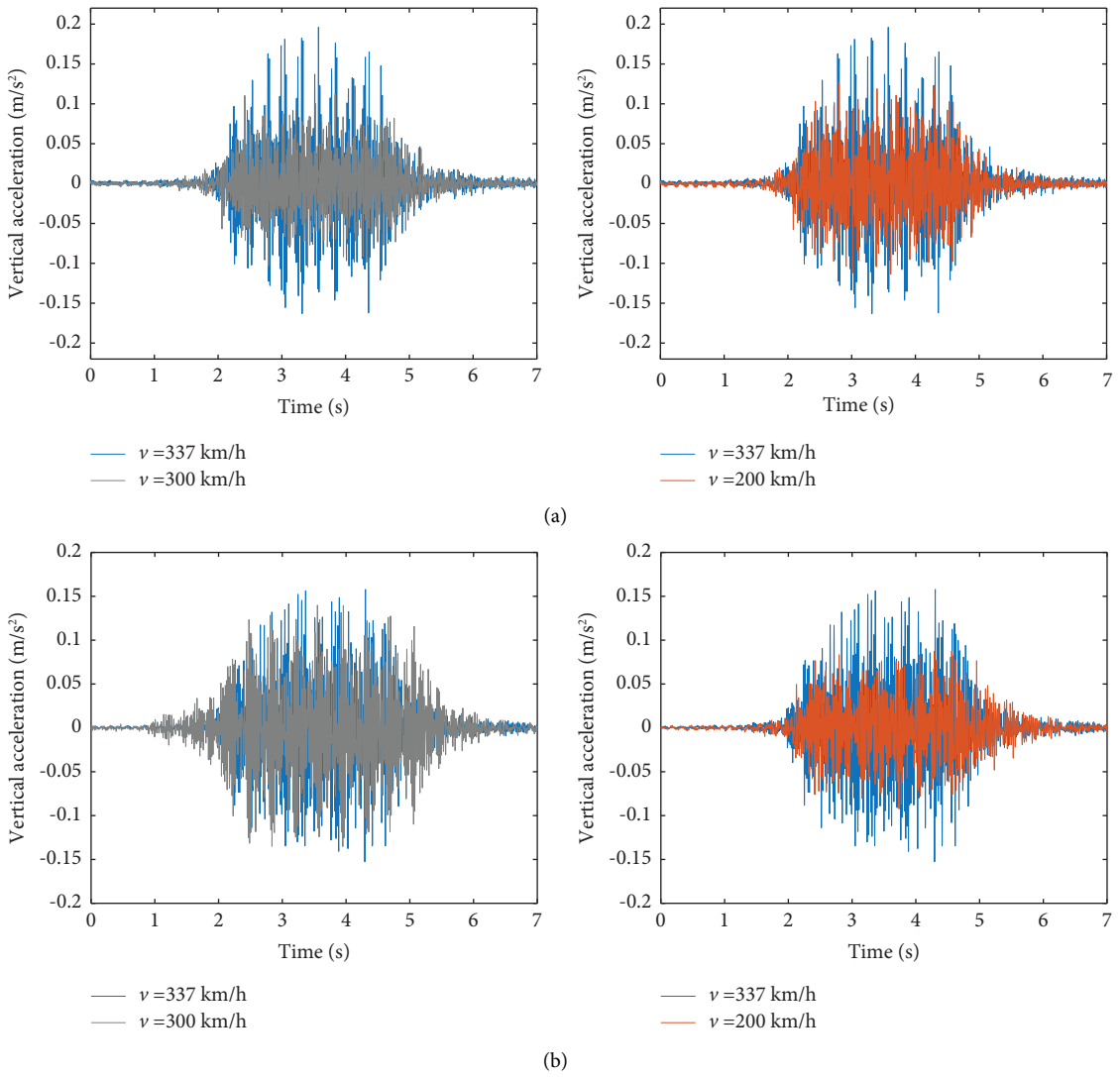

Figure 10: Comparison of ground vibrations at different train speeds. (a) $D = 11$ m. (b) $D = 16$ m.

a phenomenon that is related to the composition of train vehicles.

In Figure 15, it is also obvious that the energy decays with the distance increasing. The decay ranges from beam bottom to ground surface and from $D = 1$ m to $D = 6$ m is larger. The total energy from $D = 6$ m to $D = 40$ m decays continuously, but the decay range is much smaller than that from the closer distance.

In order to further reflect the distribution of vibration energy in the low-frequency band, the vibration acceleration response at $D = 1$ m, $D = 6$ m, $D = 11$ m, $D = 16$ m, $D = 24$ m, $D = 32$ m, and $D = 40$ m is analyzed by 1/3 octave band spectra. Take the ground vibrations at train speed v = 337km/h as an example, the vertical vibration acceleration levels in the 1/3 octave band are shown in Figure 16 in the form of a broken line diagram and ladder diagram, respectively.

It can be seen from Figure 16 that the vibration acceleration level has peak values in the central frequency bands of 4 Hz, 12.5 Hz, and 50 Hz, which is consistent with the previous time-frequency analysis. In addition, for low-frequency components below 8 Hz, the vibration acceleration level shows significant attenuation from $D = 0$ m at beam bottom to $D = 11$ m on the ground, while the

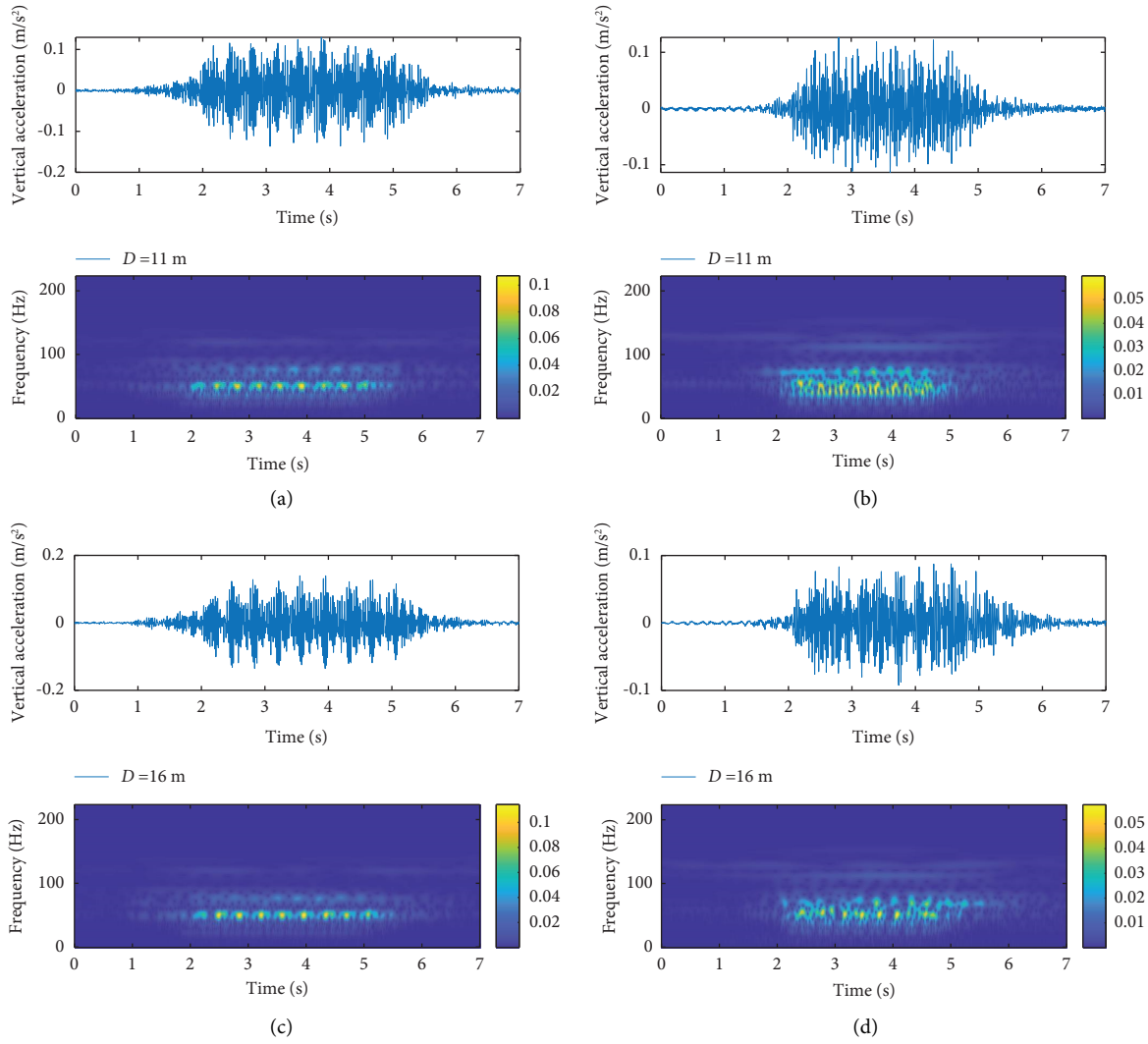

FIGURE 11: Time-frequency diagrams of ground vibration at $v = 200$ km/h and $v = 300$ km/h. (a) $D = 11$ m ($v = 200$ km/h). (b) $D = 11$ m ($v = 300$ km/h). (c) $D = 16$ m ($v = 200$ km/h). (d) $D = 16$ m ($v = 300$ km/h).

attenuation from $D = 11$ m to $D = 40$ m gradually slows down and tends to stabilize. The high-frequency components above 50 Hz rapidly decay with distance, while frequency components within the range of 8–50 Hz decay slower. This corresponds well to the conclusion in Sections 4.2.2 and 4.3. Moreover, the vibration energy continuously increases with

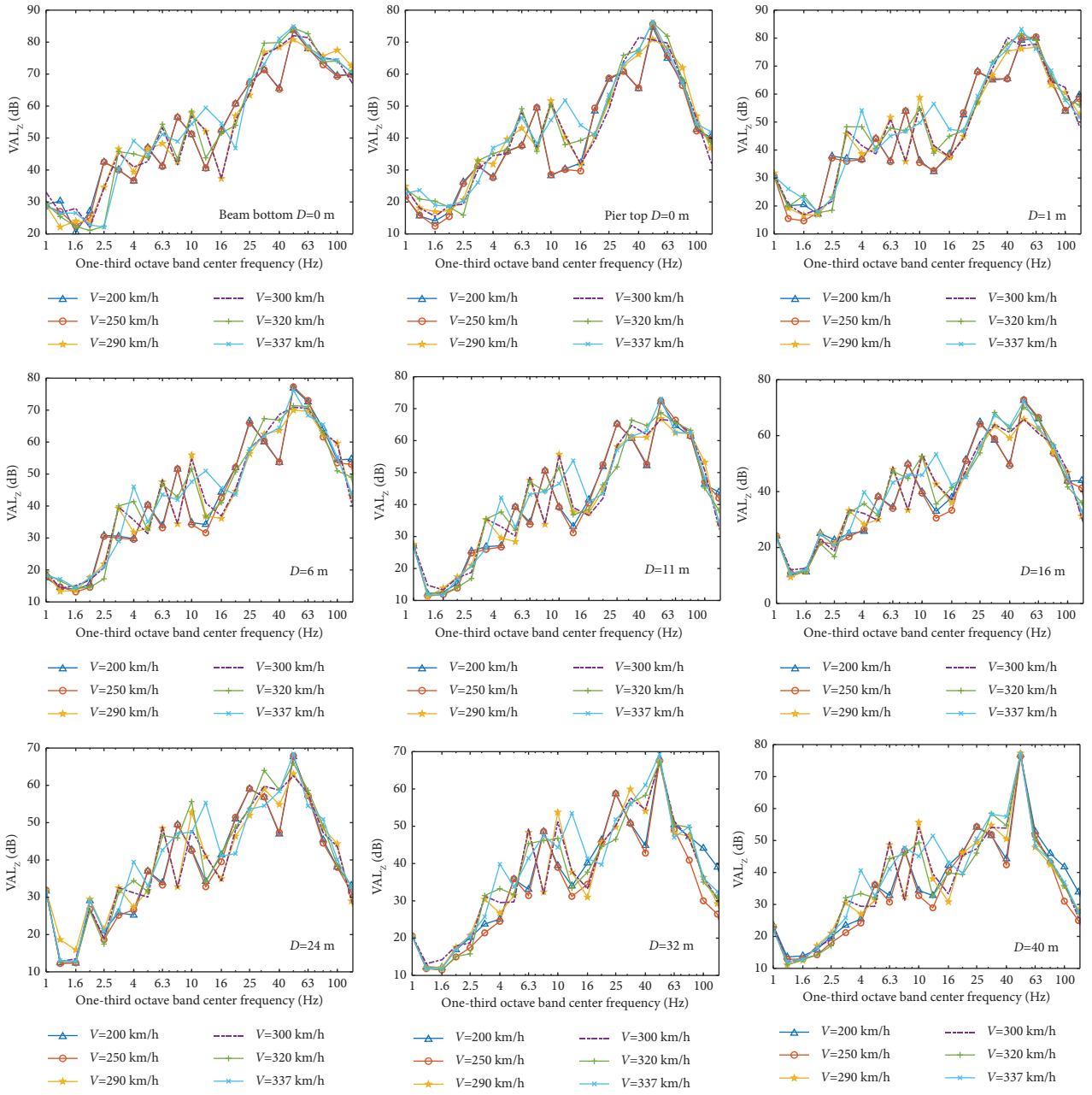

Figure 12: One-third octave spectrum of ground vibrations at different train speeds.

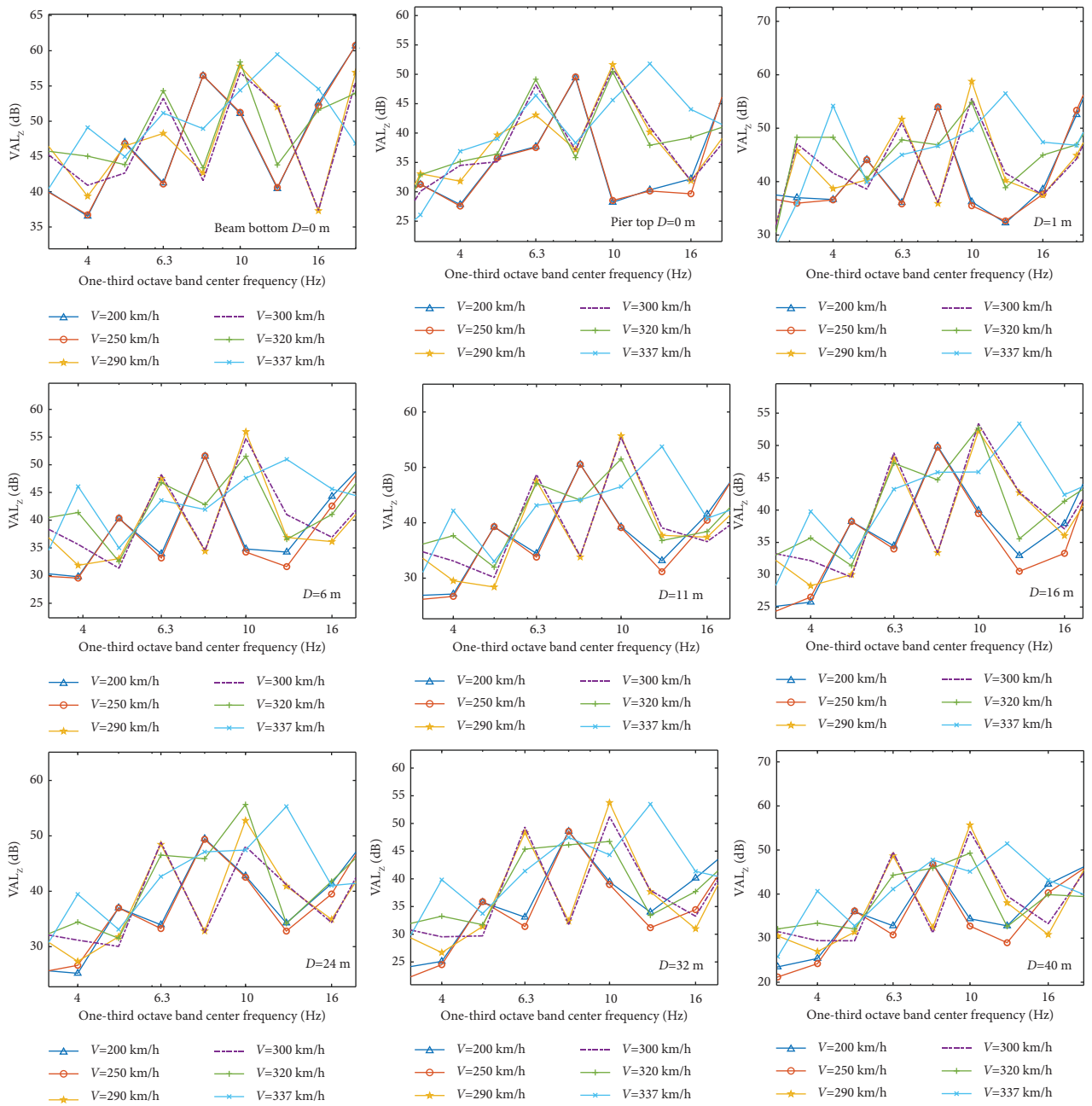

Figure 13: Local amplification of 4–16 Hz in one-third octave spectrum.

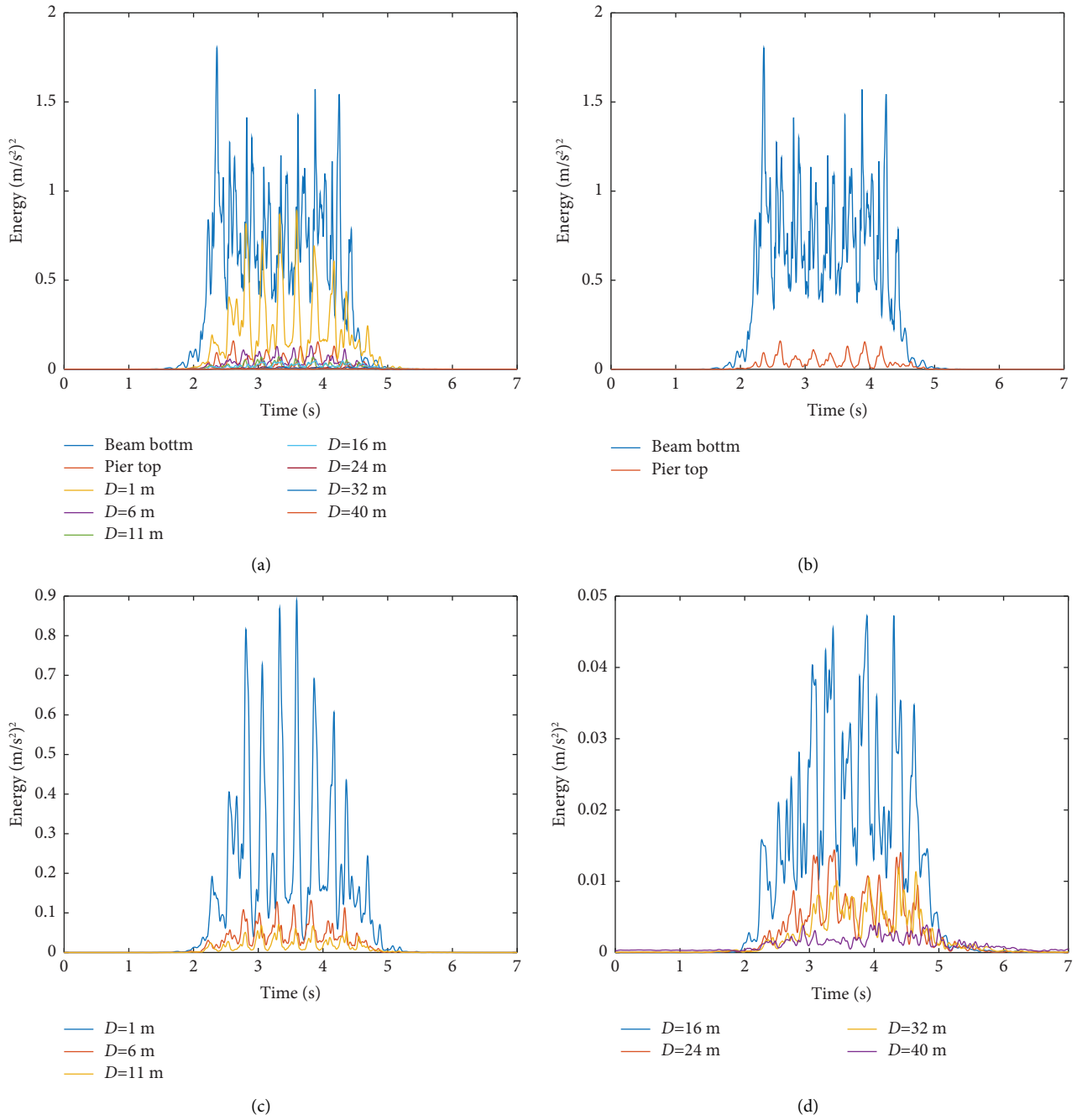

FIGURE 14: Wavelet energy diagrams at each single moment ($v = 337$ km/h). (a) All measuring points. (b) Beam bottom and pier top. (c) $D = 1$ m to $D = 11$ m. (d) $D = 16$ m to $D = 40$ m.

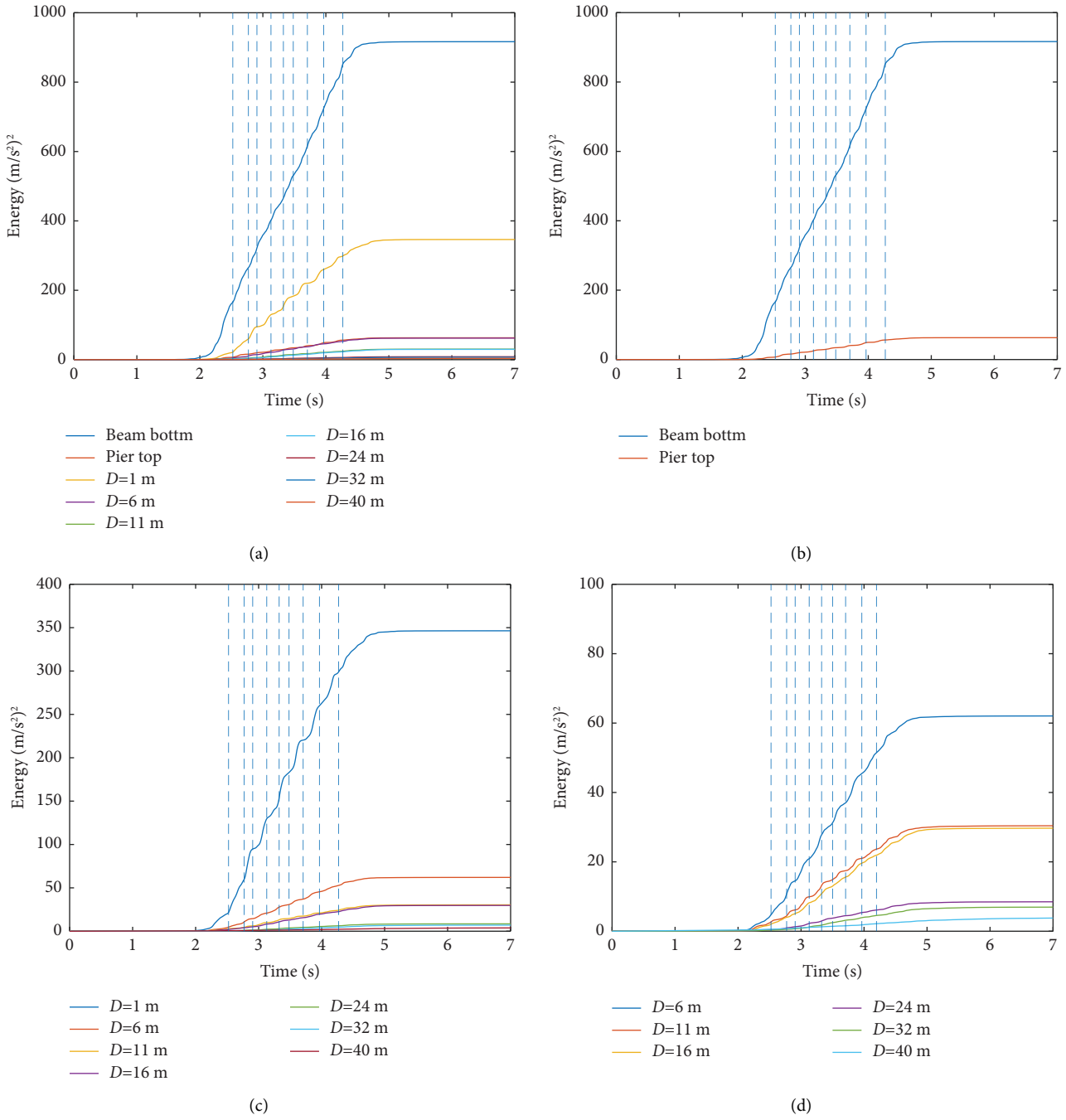

Figure 15: Wavelet energy cumulative curve ($v = 337$ km/h). (a) All measuring points. (b) Beam bottom and pier top. (c) $D = 1$ m to $D = 40$ m. (d) $D = 6$ m to $D = 40$ m.

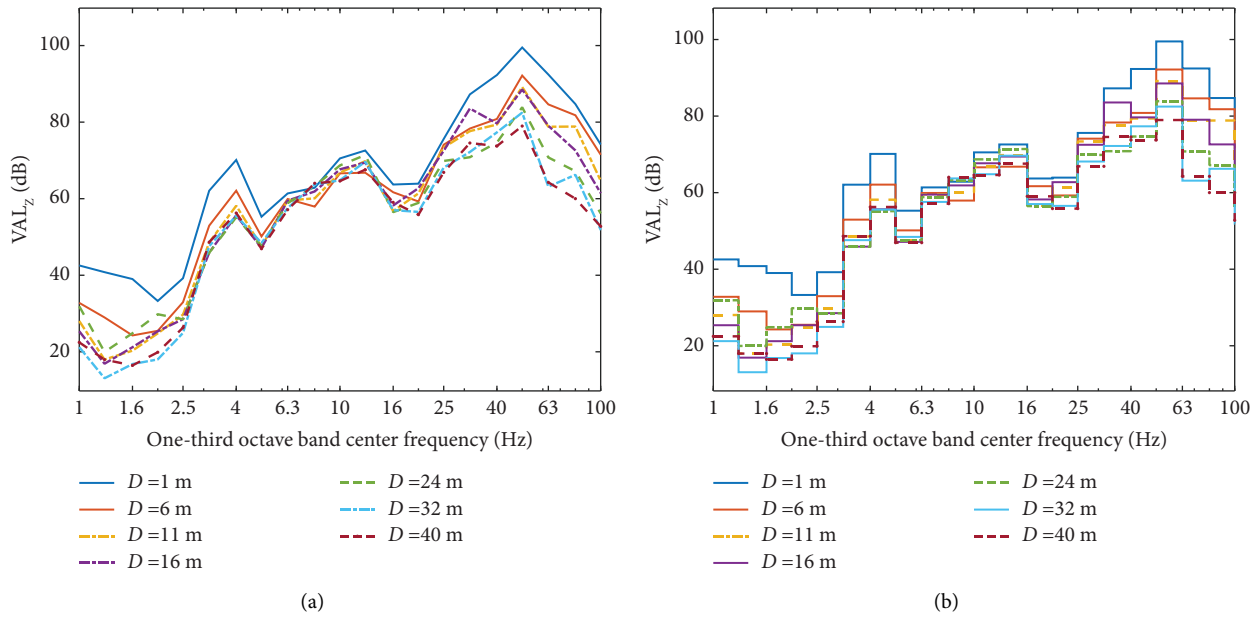

Figure 16: One-third octave band spectra of vertical acceleration level (VAL). (a) Broken line diagram. (b) Ladder diagram.

frequency in the low-frequency range of 1 to 50 Hz and shows a decreasing trend in the high-frequency range greater than 50 Hz.

5. Conclusion

In this paper, the environmental vibration caused by the viaduct section of Daxi HSR is measured, and the experimental acceleration response signals of the beam, pier, and site soil are obtained. By the analysis of time domain, frequency domain, time-frequency domain, and time-frequency energy, the following conclusions can be obtained:

(1) The vibration response of each measuring point has obvious nonstationary characteristics. The peak frequencies of the ground vibration are mainly influenced by the excitation frequencies of the axles and the peak frequencies of the wheel-rail forces. The periodic loading from the train is obvious at the ground observation point near the centerline of the pier, while it is not obvious at the far observation point due to the influence of ambient vibration.

(2) The high-frequency components with 50–100 Hz of the ground vibrations will rapidly decay with increasing distance. The low-frequency components with 0–8 Hz decay faster near the vibration source, while the middle-frequency components with 8–50 Hz decay slowest and can propagate further, playing a dominant role in the far-field frequency components. The variation relationship between vibration response and frequency at different train speeds can maintain good consistency before 4 Hz and after 16 Hz, but between 4 Hz and 16 Hz, the influence of train speed on ground vibration is obvious.

(3) The ground-borne vibration has a discontinuous localized concentration band corresponding to train formation, so the time-frequency energy analysis of the signal is a more accurate description in dealing with the problem of environmental vibration induced by railway traffic.

The CWT makes a great contribution to the mutual correspondence of time and frequency and can provide more accurate and intuitive analysis in the time-frequency domain than the traditional Fourier transform. So, it is a promising analysis tool for studying ground vibrations induced by elevated HSR train.

Data Availability

All the data in this article are obtained by the author's field measurement. If necessary, please contact the author by email.

Disclosure

A preprint has previously been published (Cao, Yanmei and Xiang, Qi and Li, Boyang and Li, Zhaoyang, Field Measurement and Energy Analysis of Ground-Borne Vibration around High-Speed Railway Viaduct which is available at SSRN: https://ssrn.com/abstract=4410586 or https://doi.org/10.2139/ssrn.4410586).

Conflicts of Interest

The authors declare that they have no conflicts of interest.

Acknowledgments

The research was supported by the grant of Natural Science Foundation of Beijing Municipality (8222024).

References

[1] D. P. Connolly, G. P. Marecki, G. Kouroussis, I. Thalassinakis, and P. K. Woodward, "The growth of railway ground vibration problems-A review," *Science of the Total Environment*, vol. 568, pp. 1276–1282, 2016.

[2] M. G. Smith, I. Croy, M. Ögren, and K. Persson Waye, "On the influence of freight trains on humans: a laboratory investigation of the impact of nocturnal low frequency vibration and noise on sleep and heart rate," *PLoS One*, vol. 8, no. 2, Article ID e55829, 2013.

[3] M. G. Smith, I. Croy, M. Ögren, O. Hammar, E. Lindberg, and K. Persson Waye, "Physiological effects of railway vibration and noise on sleep," *Journal of the Acoustical Society of America*, vol. 141, no. 5, pp. 3262–3269, 2017.

[4] S. Qu, L. Zhao, J. Yang, Z. Wu, S. Zhu, and W. Zhai, "Numerical analysis of engineered metabarrier effect on ground vibration induced by underground high-speed train," *Soil Dynamics and Earthquake Engineering*, vol. 164, Article ID 107580, 2023.

[5] Y. W. Gu, X. Nie, A. G. Yan, J. H. Zeng, Y. F. Liu, and Y. X. Jiang, "Experimental and numerical study on vibration and structure-borne noise of high-speed railway composite bridge," *Applied Acoustics*, vol. 192, Article ID 108757, 2022.

[6] Z. Zhang, X. Li, X. Zhang, J. Fan, and G. Xu, "Semi-analytical simulation for ground-borne vibration caused by rail traffic on viaducts: vibration-isolating effects of multi-layered elastic supports," *Journal of Sound and Vibration*, vol. 516, Article ID 116540, 2022.

[7] A. Colaço, A. Castanheira Pinto, P. Alves Costa, and J. Fernández Ruiz, "Combination of experimental measurements and numerical modelling for prediction of ground-borne vibrations induced by railway traffic," *Construction and Building Materials*, vol. 343, Article ID 127928, 2022.

[8] H. Xia, J. G. Chen, C. Y. Xia, H. Inoue, Y. Zenda, and L. Qi, "An experimental study of train-induced structural and environmental vibrations of a rail transit elevated bridge with ladder tracks," *Proceedings of the Institution of Mechanical Engineers–Part F: Journal of Rail and Rapid Transit*, vol. 224, no. 3, pp. 115–124, 2010.

[9] W. Zhai, K. Wei, X. Song, and M. Shao, "Experimental investigation into ground vibrations induced by very high speed trains on a non-ballasted track," *Soil Dynamics and Earthquake Engineering*, vol. 72, pp. 24–36, 2015.

[10] D. Niu, Y. Deng, H. Mu, J. Chang, Y. Xuan, and G. Cao, "Attenuation and propagation characteristics of railway load-induced vibration in a loess area," *Transportation Geotechnics*, vol. 37, Article ID 100858, 2022.

[11] P. Wang, K. Wei, L. Wang, and J. Xiao, "Experimental study of the frequency-domain characteristics of ground vibrations caused by a high-speed train running on non-ballasted track," *Proceedings of the Institution of Mechanical Engineers–Part F: Journal of Rail and Rapid Transit*, vol. 230, no. 4, pp. 1131–1144, 2016.

[12] L. Wang, P. Wang, K. Wei, R. Dollevoet, and Z. Li, "Ground vibration induced by high speed trains on an embankment with pile-board foundation: modelling and validation with in situ tests," *Transportation Geotechnics*, vol. 34, Article ID 100734, 2022.

[13] W. Li and W. Liu, "A novel formulation for transfer path identification and vibration prediction in the over-track building induced by trains," *Environmental Science and Pollution Research*, vol. 30, 2023.

[14] W. Liu, C. Li, L. Ma, and L. Du, "A frequency-domain formulation for predicting ground-borne vibration induced by underground train on curved track," *Journal of Sound and Vibration*, vol. 549, Article ID 117578, 2023.

[15] K. A. Kuo, H. Verbraken, G. Degrande, and G. Lombaert, "Hybrid predictions of railway induced ground vibration using a combination of experimental measurements and numerical modelling," *Journal of Sound and Vibration*, vol. 373, pp. 263–284, 2016.

[16] K. A. Kuo, M. Papadopoulos, G. Lombaert, and G. Degrande, "The coupling loss of a building subject to railway induced vibrations: numerical modelling and experimental measurements," *Journal of Sound and Vibration*, vol. 442, pp. 459–481, 2019.

[17] A. Colaço, D. Barbosa, and P. Alves Costa, "Hybrid soil-structure interaction approach for the assessment of vibrations in buildings due to railway traffic," *Transportation Geotechnics*, vol. 32, Article ID 100691, 2022.

[18] D. P. Connolly, G. Kouroussis, A. Giannopoulos, O. Verlinden, P. K. Woodward, and M. C. Forde, "Assessment of railway vibrations using an efficient scoping model," *Soil Dynamics and Earthquake Engineering*, vol. 58, pp. 37–47, 2014.

[19] G. Paneiro, F. O. Durão, M. Costa e Silva, and P. Falcão Neves, "Artificial neural network model for ground vibration amplitudes prediction due to light railway traffic in urban areas," *Neural Computing & Applications*, vol. 29, no. 11, pp. 1045–1057, 2018.

[20] R. Liang, W. Liu, C. Li, W. Li, and Z. Wu, "A novel efficient probabilistic prediction approach for train-induced ground vibrations based on transfer learning," *Journal of Vibration and Control*, pp. 1–12, Article ID 107754632211487, 2023.

[21] A. Bosse, F. Tasker, and S. Fisher, "Real-time modal parameter estimation using subspace methods: applications," *Mechanical Systems and Signal Processing*, vol. 12, no. 6, pp. 809–823, 1998.

[22] F. Tasker, A. Bosse, and S. Fisher, "Real-time modal parameter estimation using subspace methods: theory," *Mechanical Systems and Signal Processing*, vol. 12, no. 6, pp. 797–808, 1998.

[23] A. Caprioli, A. Cigada, and D. Raveglia, "Rail inspection in track maintenance: a benchmark between the wavelet approach and the more conventional Fourier analysis," *Mechanical Systems and Signal Processing*, vol. 21, no. 2, pp. 631–652, 2007.

[24] A. Garinei, G. Risitano, L. Scappaticci, and F. Castellani, "An optimized method to evaluate the performance of trench isolation for railway-induced vibration," *Measurement*, vol. 94, pp. 92–102, 2016.

[25] L. Wang, M. McCullough, and A. Kareem, "Modeling and simulation of nonstationary processes utilizing wavelet and Hilbert transforms," *Journal of Engineering Mechanics*, vol. 140, no. 2, pp. 345–360, 2014.

[26] S. Laflamme, J. J. E. Slotine, and J. J. Connor, "Wavelet network for semi-active control," *Journal of Engineering Mechanics*, vol. 137, no. 7, pp. 462–474, 2011.

[27] C. Tan, A. Elhattab, and N. Uddin, "Drive-by" bridge frequency-based monitoring utilizing wavelet transform," *Journal of Civil Structural Health Monitoring*, vol. 7, no. 5, pp. 615–625, 2017.

[28] T. Asada, C. Roberts, and T. Koseki, "An algorithm for improved performance of railway condition monitoring equipment: alternating-current point machine case study,"

Transportation Research Part C: Emerging Technologies, vol. 30, pp. 81–92, 2013.

[29] Y. Christos, M. Jedrzej, R. Konstantinos, and A. Ioannis, "Multicomponent decomposition of a time-varying acoustic Doppler signal generated by a passing railway vehicle using Complex Shifted Morlet Wavelets," *Transportation Research Part C: Emerging Technologies*, vol. 44, pp. 34–51, 2014.

[30] B. Liang, S. D. Iwnicki, Y. Zhao, and D. Crosbee, "Railway wheel-flat and rail surface defect modelling and analysis by time-frequency techniques," *Vehicle System Dynamics*, vol. 51, no. 9, pp. 1403–1421, 2013.

[31] H. Tsunashima and R. Hirose, "Condition monitoring of railway track from car-body vibration using time-frequency analysis," *Vehicle System Dynamics*, vol. 60, no. 4, pp. 1170–1187, 2022.

[32] Y. M. Hsueh, V. R. Ittangihal, W. B. Wu, H. C. Chang, and C. C. Kuo, "Fault diagnosis system for induction motors by CNN using empirical wavelet transform," *Symmetry*, vol. 11, no. 10, p. 1212, 2019.

[33] Y. Liao, X. Zeng, and W. Li, "Wavelet transform based convolutional neural network for gearbox fault classification," in *Proceedings of the 2017 Prognostics and System Health Management Conference (PHM-Harbin)*, pp. 1–6, IEEE, Harbin, China, July 2017.

[34] D. Cantero, M. Ülker-Kaustell, and R. Karoumi, "Time-frequency analysis of railway bridge response in forced vibration," *Mechanical Systems and Signal Processing*, vol. 76-77, pp. 518–530, 2016.

[35] S. Rajasekaran, V. Latha, and S. C. Lee, "Generation of artificial earthquake motion records using wavelets and principal component analysis," *Journal of Earthquake Engineering*, vol. 10, no. 5, pp. 665–691, 2006.

[36] A. A. Chanerley and N. A. Alexander, "Obtaining estimates of the low-frequency 'fling', instrument tilts and displacement time series using wavelet decomposition," *Bulletin of Earthquake Engineering*, vol. 8, no. 2, pp. 231–255, 2010.

[37] S. Yaghmaei Sabegh, "Application of wavelet transforms on characterization of inelastic displacement ratio spectra for pulse-like ground motions," *Journal of Earthquake Engineering*, vol. 16, no. 4, pp. 561–578, 2012.

[38] Z. Zhou and H. Adeli, "Wavelet energy spectrum for time-frequency localization of earthquake energy," *International Journal of Imaging Systems and Technology*, vol. 13, no. 2, pp. 133–140, 2003.

[39] I. Daubechies, *Ten Lectures on Wavelets*, Society for Industrial and Applied Mathematics, Philadelphia, PA, USA, 1992.

[40] P. Liang, C. Deng, J. Wu, Z. Yang, J. Zhu, and Z. Zhang, "Compound fault diagnosis of gearboxes via multi-label convolutional neural network and wavelet transform," *Computers in Industry*, vol. 113, Article ID 103132, 2019.

[41] M. Ülker-Kaustell and R. Karoumi, "Application of the continuous wavelet transform on the free vibrations of a steel-concrete composite railway bridge," *Engineering Structures*, vol. 33, no. 3, pp. 911–919, 2011.

[42] W. Liu, R. Liang, H. Zhang, Z. Wu, and B. Jiang, "Deep learning based identification and uncertainty analysis of metro train induced ground-borne vibration," *Mechanical Systems and Signal Processing*, vol. 189, Article ID 110062, 2023.

[43] H. Xia, N. Zhang, and W. Guo, *Dynamic Interaction of Train-Bridge Systems in High-Speed Railways*, Springer, Berlin, Germany, 2018.

[44] ISO, *International Standard, ISO 14837-1: Mechanical vibration--Ground-borne noise and vibration arising from rail systems–Part1: General guidance*, ISO, Geneva, Switzerland, 1st edition, 2005.

[45] ISO, *International Standard, ISO8041-1: Human Response to Vibration-Measuring Instrumentation Part1: General Purpose Vibration Meters*, ISO, Geneva, Switzerland, 1st edition, 2017.

[46] L. Auersch, "Ground vibration due to railway traffic-The calculation of the effects of moving static loads and their experimental verification," *Journal of Sound and Vibration*, vol. 293, no. 3-5, pp. 599–610, 2006.

[47] L. Auersch, "Train-induced ground vibration due to the irregularities of the soil," *Soil Dynamics and Earthquake Engineering*, vol. 140, Article ID 106438, 2021.

[48] L. Auersch, "The excitation of ground vibration by rail traffic: theory of vehicle-track-soil interaction and measurements on high-speed lines," *Journal of Sound and Vibration*, vol. 284, no. 1-2, pp. 103–132, 2005.

[49] Q. Li and D. J. Wu, "Analysis of the dominant vibration frequencies of rail bridges for structure-borne noise using a power flow method," *Journal of Sound and Vibration*, vol. 332, no. 18, pp. 4153–4163, 2013.

[50] S. H. Ju, H. T. Lin, and J. Y. Huang, "Dominant frequencies of train-induced vibrations," *Journal of Sound and Vibration*, vol. 319, no. 1-2, pp. 247–259, 2009.